Mechanism of Secondary Hardening in Rapid Tempering of Dual-Phase Steel

DULAL CHANDRA SAHA, SASHANK S. NAYAK, ELLIOT BIRO,
ADRIAN P. GERLICH, and Y. ZHOU

Dual-phase steel with ferrite-martensite-bainite microstructure exhibited secondary hardening in the subcritical heat affected zone during fiber laser welding. Rapid isothermal tempering conducted in a Gleeble simulator also indicated occurrence of secondary hardening at 773 K (500 °C), as confirmed by plotting the tempered hardness against the Holloman–Jaffe parameter. Isothermally tempered specimens were characterized by analytic transmission electron microscopy and high-angle annular dark-field imaging. The cementite (Fe_3C) and TiC located in the bainite phase of DP steel decomposed upon rapid tempering to form needle-shaped Mo_2C (aspect ratio ranging from 10 to 25) and plate-shaped M_4C_3 carbides giving rise to secondary hardening. Precipitation of these thermodynamically stable and coherent carbides promoted the hardening phenomenon. However, complex carbides were only seen in the tempered bainite and were not detected in the tempered martensite. The martensite phase decomposed into ferrite and spherical Fe_3C, and interlath-retained austenite decomposed into ferrite and elongated carbide.

DOI: 10.1007/s11661-014-2591-8

I. INTRODUCTION

DUAL-PHASE (DP) steel is composed of soft ferrite (α) matrix mixed with hard martensite (α') islands. This microstructure leads to its high strength and excellent ductility, which is why it has been so widely adopted for automotive construction resulting in reductions in vehicle weight and improvements in fuel economy. The strength of DP steel is determined by the volume fraction of martensite within its structure.[1] Although DP steels can be used to produce high-strength components with lower sheet thicknesses than conventional steels, it has also been reported that a decrease in hardness occurs in DP steels after welding, which is commonly termed as heat-affected zone (HAZ) softening.[2–4] Softening occurs when the martensite within the DP microstructure is tempered. In welding applications, softening has been reported to deteriorate weld mechanical properties compared to the base metal.[5–10] In the case of high-strength martensitic steels, this is a challenge as the softened zones may lead to failure in-service or during forming at stress levels far below the ultimate tensile strength (UTS) of the base material.

Martensite tempering is a multistage process that is generally performed to enhance the ductility and toughness of quenched steels with martensitic microstructures. In the first stage of tempering, at temperatures ranging from 353 K to 453 K (80 °C to 180 °C), segregation and redistribution of carbon atoms occur at lattice defects—carbon clusters—and transitional carbides, especially ε-carbide ($Fe_{2.4}C$), are formed.[11–13] However, it should be noted that transitional carbides typically only precipitate when the C content of the steel exceeds 0.2 pct. Retained austenite, which is sometimes present at the interlath area of the martensite structure, decomposes into ferrite and cementite between the temperatures ranging from 473 K to 573 K (200 °C to 300 °C) during the second stage of tempering.[12] In the third stage of tempering, segregated carbon and transitional carbides transform into cementite (Fe_3C). This occurs at higher temperatures ranging from 523 K to 623 K (250 °C to 350 °C).[12]

Reduction of hardness in the tempered area of the HAZ is directly influenced by the phase fraction of martensite in the base material. It was reported that fully martensite-containing steel is prone to severe softening during tempering. Therefore, we attempted to modify microstructure of the DP steels by the addition of suitable minor alloying elements such as Cr, Mo, V, and Nb to get better combination of strength and ductility. Thus, DP780 steel was produced with ferrite, martensite, and bainite phases to investigate the effect of bainite constituents on rapid tempering processes, such as laser welding process.

Although hardness is expected to decrease when martensite-containing steels are tempered,[2–10] the authors' recent study has shown that the lower temperature (below the Ac_1 temperature, the critical temperature at which austenite begins to form on heating) areas of the HAZ of diode laser welds in bainite (α_b)-containing DP780 steel will sometimes show an increase in hardness, although softening would be expected.[14]

DULAL CHANDRA SAHA, Ph.D. Student, SASHANK S. NAYAK, Research Associate, ADRIAN P. GERLICH, Associate Professor, and Y. ZHOU, Professor, are with the Department of Mechanical and Mechatronics Engineering, University of Waterloo, 200 University Avenue West, Waterloo, ON N2L 3G1, Canada. Contact e-mail: dcsaha@uwaterloo.ca ELLIOT BIRO, Manager Product Characterization, is with the ArcelorMittal Global Research, 1390 Burlington Street East, Hamilton, ON L8N 3J5, Canada.

Manuscript submitted January 13, 2014.

This hardness increase has been determined to be secondary hardening,[14] which has been observed in martensitic steels containing carbide formers such as Mo and Cr after prolonged (over 1 hour) tempering at about 773 K (500 °C).[15–18] Secondary hardening occurs because cementite dissolves within the structure, while being replaced with alloy carbides, such as Mo_2C and VC, which are reported to be the cause of secondary hardening. In previous studies, it was observed that α' was transformed into α-ferrite and cementite. As tempering time progresses, the cementite dissolves, and carbon turns into solid solution before forming Mo_2C and VC.[15]

The present study reports the mechanism responsible for secondary hardening observed in rapidly tempered, *i.e.*, Gleeble heat-treated and laser-welded DP780 with a ferrite-martensite-bainite microstructure. The changes in hardness are explained by observing the microstructural changes in the steel using transmission electron microscopy (TEM) and high-angle annular dark-field (HAADF) imaging.

II. EXPERIMENTAL

The present study examines a 1.35-mm-thick DP780 (UTS ≥ 780 MPa) steel with a ferrite-martensite-bainite microstructure, which is used in the present study. The chemical composition of the steel is listed in Table I, and its mechanical properties are shown in Table II.

The steel was welded using an IPG Photonics Ytterbium Fiber Laser System (YLS-6000-S2) with a fiber core diameter of 0.3 mm. The fiber was fed into a laser head with a focal length of 200 mm and produced a spot diameter of 0.6 mm. Laser welding was carried out at a welding power of 6 kW and a speed of 14 m/min. These parameters resulted in a rapid thermal cycle (heating rate: 20,000 K/s and cooling rate: 10,000 K/s as calculated using Rosenthal equation[19]). No shielding gas was used in this study; instead, blown air was used to remove vapors from the weld pool, and keyhole, as well as to protect the system optics. Rapid tempering of the steel was done using a Gleeble 3500 thermomechanical simulator. To ensure the proper gripping with copper clamps, 5-mm diameter holes were made along the longitudinal directions, which were about 7.5 mm apart from the ends of the coupons. The zinc coating was removed from the samples before Gleeble heat treatment, by dipping them in a 1:1 volumetric solution of hydrochloric (HCl) acid. Then, a K-type thermocouple (alumel and chromel) was welded to the center of the specimen (inset of Figure 1). Further thermocouple was welded 20 mm away from the specimen center to ensure the uniformity of the heat treatment. The thermocouples were shielded with an aluminum oxide shield near the contact points to prevent melting or shorting. The temperature history recorded during rapid tempering in Gleeble is illustrated in Figure 1. Heating rate between 1,500 and 2,000 K/s was used to temper the specimens between 673 K and 923 K (400 °C and 650 °C) for 0.2, 0.5, 1, 2, and 10 seconds, which were then quenched in water with cooling rates ranging from 5,000 to 10,000 K/s.

A Clemex JS-200 automated computerized hardness tester was used to measure the Vickers microhardness for both the welded and the heat-treated samples using an indenter load of 200 g and a 15 seconds dwell time. Sufficient distance (150 μm) was maintained between consecutive indentations to avoid interference from adjacent stain fields. TEM was used to characterize the microstructure using a JEOL 2010F (Japan Electron Optics Ltd., Tokyo, Japan) electron microscope operated at 200 kV. Both twin-jet electropolished thin foils and carbon replicas were examined by TEM. The

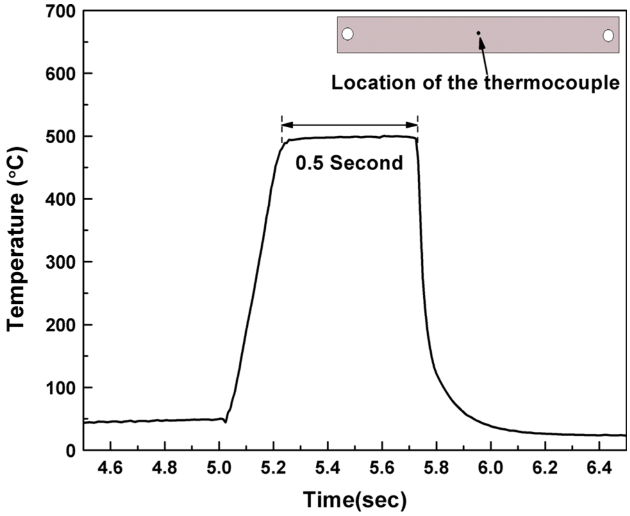

Fig. 1—Thermal cycle involved in Gleeble rapid tempering of DP780 steel (inset location of the thermocouples in the Gleeble sample).

Table I. Chemical Compositions of the Experimental Dual-Phase Steel (in Weight Percent)

Steel	C	Mn	Si	Al_{total}	Ti	V	Ni	Cu	Cr	Mo	Nb	B	N	P	S
DP780	0.140	1.91	0.286	0.026	0.024	0.004	0.020	0.018	0.247	0.104	0.001	0.0003	0.0098	0.015	0.002

Table II. Mechanical Properties of Experimental Dual-Phase Steel

Steel	UTS	0.2 pct Proof Strength (MPa)	Uniform Elongation (pct)	Total Elongation (pct)
DP780	763.10	485.45	10.70	19.23

twin-jet electropolished samples were prepared by punching out 3-mm disks from samples that were mechanically ground to the sizes ranging from 40 to 50 μm. The disks were thinned in a Struers Tenupol-5 twin-jet electropolishing unit using a 10 pct $HClO_4$ and 90 pct ethanol electrolyte maintained at -318 K (-45 °C) while maintaining a voltage of 15 V. To prepare the carbon replica samples, a thin carbon film was deposited on the surface of the etched (2 pct nital solution) samples. The carbon film was then sectioned into small square pieces using a razor. The specimen with sectioned carbon film was immersed inside 4 pct nitric acid in ethanol solution to float the pieces of carbon films, which were then collected on to copper grids and allowed to dry before observing under microscope.

III. RESULTS AND DISCUSSION

The SEM micrograph of the steel used in this study is illustrated in Figure 2. The DP780 steel contains 63 pct α (the dark phase) and 24 pct α' islands (the white phase) with an additional 13 pct α_b constituent. The volume fraction of each phase was estimated using SEM imaging at 2000× magnification and manually outlining each representative phase, which was identified by its contrast and morphology. To obtain an accurate volume fraction, approximately 500 grains were used. Each image was able to capture up to approximately 35 grains; 15 SEM images were used to estimate the volume fraction. It can be noted that the strength of DP steels is determined by the volume fraction of martensite or bainite.[20] For example, DP steel having UTS of about 980 MPa contains 52 pct martensite; conversely, 24 pct martensite-containing DP steels have UTS of about 780 MPa. It was reported that DP steel composed of bainite constituent provides better ductility and lower strength compared with only martensite-containing DP steels.[21] The typical lath structure can be observed inside of each α' island. Retained austenite was also found between the martensite laths (interlath region). The α_b phase contains bainitic ferrite plates separated by cementite.

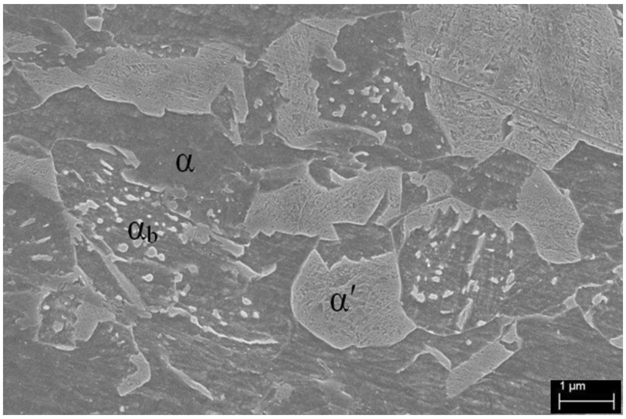

Fig. 2—SEM micrographs of the as-received DP780 steel showing ferrite (α) matrix with combination of martensite (α') and bainite (α_b) phases.

Figure 3 illustrates the microhardness profile across the fiber laser-welded zone in the DP780 steel. The different areas of the weld are marked as FZ (fusion zone), HAZ, and BM (base metal). An increase in hardness was measured close to the BM on multiple welds. The increase in hardness was significantly higher than both that of the BM and the minimum HAZ hardness measured closer to the fusion boundary in the subcritical heat-affected zone (SCHAZ). This increased hardness is referred to as secondary hardening. This phenomenon was also observed in diode laser welds in the authors' previous study.[14] As similar secondary hardening trends were observed for both fiber and diode laser welding processes, it suggests that the secondary hardening phenomenon was dependent on the material, rather than on the specific laser welding process (fiber or diode). Secondary hardening in the fiber laser-welded samples was not expected, as due to the high power density ($>10^5$ W/cm^2) and travel speed of this process, the material underwent rapid tempering (with a heating rate on the order of 20,000 K/s). Typically, secondary hardening is not seen in samples tempered for short time; it has been observed only in martensitic steel tempered for longer (more than 1 hour) times at temperatures at or above 773 K (500 °C).[22] The steel investigated in this study contains minor alloying additions of Cr, Mo, V, and Nb. Therefore, it is interesting to investigate the mechanism responsible for the secondary hardening observed during rapid tempering in this DP780.

To reproduce the HAZ microstructure, the steel was tempered in a Gleeble thermomechanical simulator under a wide range of conditions. As the tempering process is influenced by both temperature and time, the tempering cycle was generalized using the Hollomon and Jaffe[23] tempering parameter, which has been used extensively to investigate the tempering response on

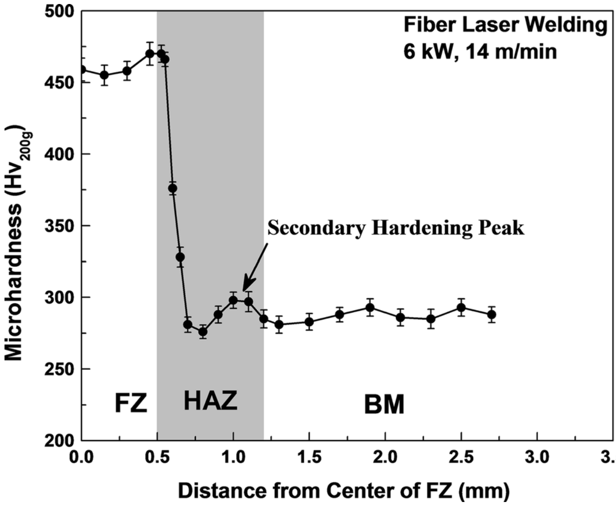

Fig. 3—Vickers microhardness profile of DP780 steel fiber laser weld (power: 6 kW, speed: 14 m/min).

hardness. The Hollomon–Jaffe (HJ) parameter is calculated using Eq. [1]:

$$P = T[c + \log(t)], \tag{1}$$

where P is the HJ tempering parameter, T is the temperature (K), c is a material constant (13 for the material used in this study[23]) and t is the holding time (seconds).

The calculated tempering parameters of Gleeble samples were plotted against their microhardness in Figure 4. When plotted, it was seen that the increase of the hardness of the tempered DP780 was a function of tempering parameter, regardless of the tempered temperature. Secondary hardening was observed at all tempering temperature; however, it was most pronounced at shorter durations (<1 second). The maximum hardening was measured at a tempering temperature of 773 K (500 °C) and over a 0.5-second duration, where the hardness increased by 8 pct with respect to the as-received material. This secondary hardening trend was consistent with the results of fiber laser-welded sample (Figure 3) where peak hardness increased by 3.5 pct with respect to the as-received material hardness. Figure 4 also shows the effects of tempering temperature and time on hardness. It can be observed that the tempered hardness was not affected by tempering duration when tempered at 673 K (400 °C). However, when the sample was tempered at 773 K (500 °C), the highest secondary hardening peak was observed at short tempering duration (0.5 second), and hardness decreased with the increasing tempering duration. It was also found that with the increasing tempering duration, the hardness values tend to decrease, which was due to coarsening of cementite particles, increasing the effective free length of dislocations and decreasing the flow stresses.[24]

The TEM micrographs of α, α′, and α_b structures of the as-received steel are shown in Figure 5(a). Twinned structure was seen inside the martensite block (marked by the dotted lines in Figure 5(b)) having packets, with unidirectional twins, oriented in a different angle. The dotted arrow represents the plane normal to the twin direction. Bright-field images of α′ and α_b structures with the corresponding selected area diffraction (SAD) patterns are illustrated in Figures 5(c) and (e), respectively. The indexed SAD pattern shows the $[011]_{\alpha'}$ zone axis, and the twinned substructures are visible inside the α′ structure. Twinned structure is typically only observed in high carbon-containing steel. The presence of twins in the α′ indicates that C was portioned from the matrix to the α′ when the DP structure was formed, increasing the C content of the α′ above that of the bulk amount. The α′ carbon content was calculated using Eq. [2]:

$$\text{pct}\, C_m = \frac{(\text{pct}\, C_s - 0.02)}{f_m + f_b} + 0.02, \tag{2}$$

where C_s and C_m are the carbon content of the bulk steel and α′ carbon content, respectively; and f_m, and f_b are the volume fractions of α′, and α_b, respectively. The C content of the α′ of the DP780 was calculated to be 0.52 wt pct, justifying that the twinned structure observed within the α′ phase.[12] Nayak *et al.*[3] also reported the twinned α′ for similar carbon- and manganese-containing DP780 steel in another study. The SAD pattern presented in Figure 5(c) also shows the double reflection of the α′ twin plates, which confirmed the existence of twin plates as expected from the calculated carbon content.

The α_b structure was also observed in the steel structure, having cementite at the boundaries of the bainitic ferrite laths (Figure 5(d)) following $[001]_\theta||[133]_\alpha$ orientation relationship. Bright-field images (Figures 6(a) and (b)) and HAADF image (Figure 6(c)) of the extracted carbon replica depicted different morphologies of the carbide precipitates: irregular spherical (nos. 1 and 4), faceted (nos. 2 and 3), and cuboid (nos. 5, and 6) shape. The sizes of the faceted shape precipitates (nos. 2, and 3) were ranging from 30 to 90 nm, whereas that of the precipitate no. 5, which exhibited cubic-shaped carbide, was about 145 nm. The SAD patterns of particles 2, 4, 5, and 6 were indexed to have a face-centered cubic (FCC) crystal structure, showing [011], $[\bar{1}23]$, [013], [001] zone axis and lattice parameters (a) of 4.27, 4.41, 4.40, and 4.31 Å, respectively. The crystal structure and lattice parameter of the particles confirmed the precipitates to be TiC, Ti(C,N), and TiN, which are known to precipitate within the α grains during thermomechanical processing of low alloy steels.[25–27] For instance, the precipitates, 5 and 2, identified to be Ti(N) and Ti(C,N), respectively, had FCC structures with the lattice parameters of 4.40 and 4.27 Å, respectively, also matching with the literature data.[25,28,29] The cubic Ti(C,N) precipitates (no. 5) exhibited a larger lattice parameter compared to the faceted shape precipitates TiC (no. 2), which is attributed to the increase in the lattice parameter when a N atom enters the TiC lattice to form Ti(C,N).[30,31] In addition, TiC (no. 6) precipitates observed with an average size of 40 nm and a lattice parameter of 4.31 Å were in agreement with the size (from 2 to 30 nm) and

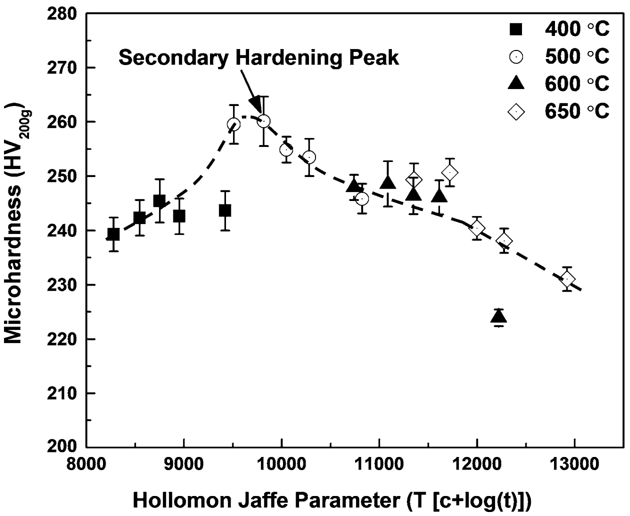

Fig. 4—Vickers microhardness profile as a function of Hollomon–Jaffe tempering parameter of Gleeble heat-treated samples for DP780 steel[14].

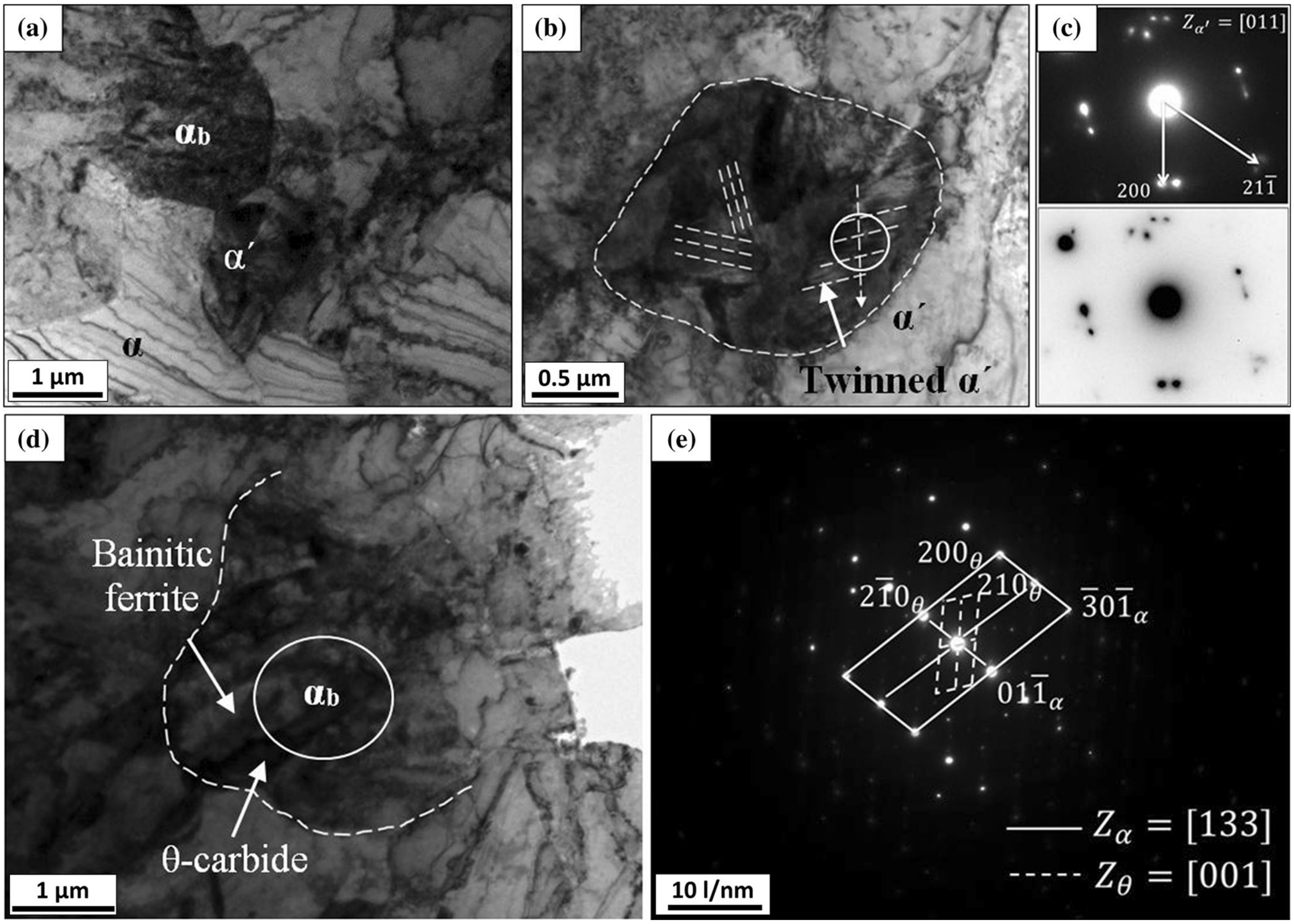

Fig. 5—The TEM micrographs of the as-received DP780 steel: (*a*) bright-field image delineating the α, α′, and α_b phases, (*b*) the α′ phase showing twinned martensite plates, (*c*) the SAD pattern taken from the area marked as circle illustrates the martensite twins reflections, (*d*) the α_b phase with bainitic ferrite plates and θ-carbides between the plates, and (*e*) indexed SAD of the bainitic ferrite and θ-carbide, where, α, α′, α_b, and θ represent ferrite, martensite, bainite, and cementite, respectively.

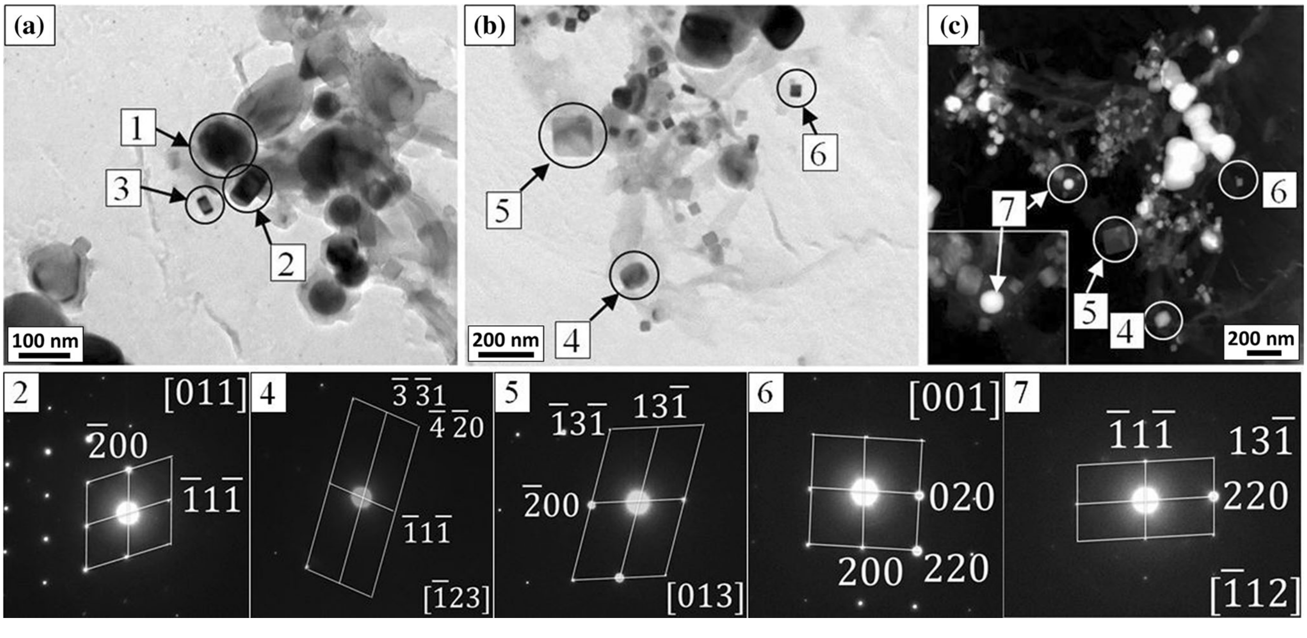

Fig. 6—The microstructures of the carbides from the as-received DP780 steel: (*a*) and (*b*) carbon-replica sample showing spherical, and faceted carbides (marked with circles), and (*c*) HAADF-STEM images of the spherical- and cuboid-shaped carbides. The selected area diffraction (SAD) patterns taken from the particles observed are also included.

lattice parameter (4.32 Å) of the TiC particles reported in the literature.[25,32] Apart from cubic and faceted TiC, TiN, and Ti(C,N) precipitates, spherical-shaped precipitates were also observed (marked as 7 in Figure 6(c)), which produced a SAD pattern showing the [$\bar{1}$12] zone axis (SAD 7) of orthorhombic crystal structure with lattice parameters of a = 4.85, b = 4.89, and c = 6.73 Å; which are close to those of orthorhombic cementite (a = 4.52, b = 5.08, and c = 6.74 Å).[16] The current observation corroborated with that of Schissler *et al.*[33] reporting the formation of orthorhombic carbides in a steel rich in silicon. The difference between the measured lattice parameters of the observed precipitates and the typical lattice parameters for cementite suggests that the observed precipitates are $(Fe,M)_3C$-type cementite, where M is Mn or Cr. The electron energy loss spectroscopy (EELS) and X-ray spectroscopy (EDX) analysis (Figure 7(a)) of the θ-carbides (inset of Figure 7(a)) confirmed the presence of peaks of the substitutional elements of Mn and Cr along with the parent Fe peak, which has also been reported by Nayak *et al.*[3] Recently, Jang *et al.*[34] have reported the changes in the lattice parameters and total volume of the cementite lattice when the Fe atoms are substituted by Mn, Si, and Al. For example, Si_3C and Al_3C showed enlarged volume of approximately 34 pct due to elongation in the b-axis compared to Fe_3C, whereas Mn_3C showed 3 pct volume reduction.[34] The α and α' phases are free from θ-carbides[16] and the θ-carbides found in the extracted replicas were confirmed to be from the bainite phase present in the used DP780 steel (Figure 5(d)). The EELS spectrum for cuboid-shaped precipitates (no. 5 in Figure 6(c)) is confirmed to be Ti(CN) as shown in Figure 7(b) (no. 5 is also shown in the inset).

TEM and scanning transmission electron microscope (STEM) images of the specimens heat treated at 773 K (500 °C) for 0.5-seconds duration showed the products of the decomposed α' and α_b structures (Figure 8), where the decomposed martensite was marked as DM, and the decomposed bainite was marked as DB. The martensite

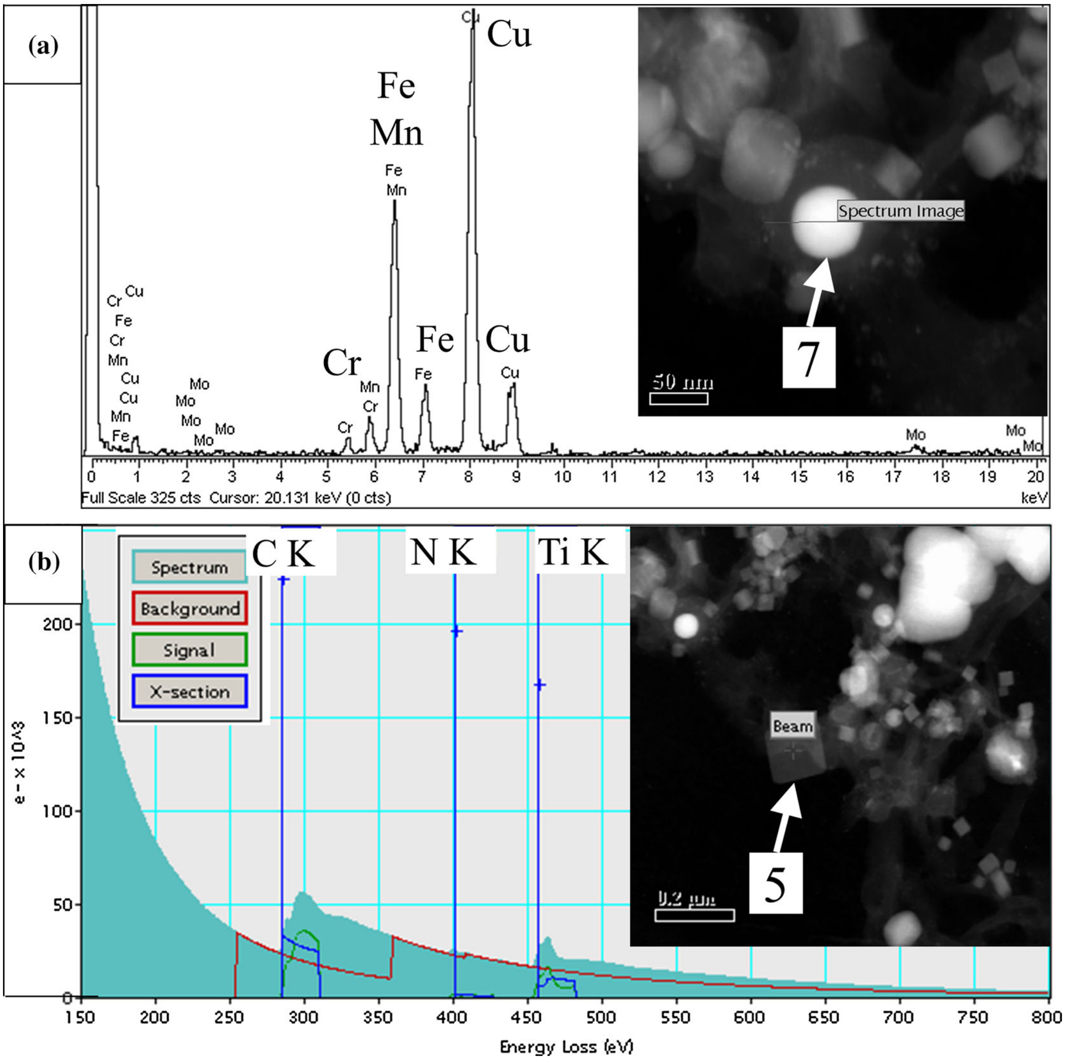

Fig. 7—Electron energy loss spectroscopy (EELS) analysis of extracted carbides from DP780 steel: (*a*) EELS spectrum indicating peaks of Fe, Mn, and Cr (inset HAADF-STEM image of cementite); and (*b*) EELS profile obtained from one of the square-shaped carbonitride, showing peaks of Ti, C, and N (inset HADDF image of the carbonitride).

structure decomposed into α and θ-carbides as seen in Figure 8(a); the spherical θ-carbides (having an average diameter of 50 ± 3 nm) are indicated by the arrows. The θ-carbides were confirmed by the SAD pattern of the θ-carbide (marked with the circle), which showed $[\bar{1}13]_\theta$ the zone axis parallel to $[\bar{1}12]_\alpha$ the zone axis of the α-matrix. The EDX analysis of the circled θ-carbides in Figures 8(a) and (b) confirmed that Cr and Mn were present within the carbide (Figure 9), and indicated that the θ-carbides had the stoichiometric form $(Fe_{0.87}Mn_{0.11}Cr_{0.02})_3C$. The θ-carbides were predominately located at the prior γ grain boundaries and block boundaries, as is commonly seen in tempered martensite.[4,35] Elongated carbides were also seen at the interlath regions of the DM structure (Figure 8(c)). The elongated carbides were formed from decomposition of the retained

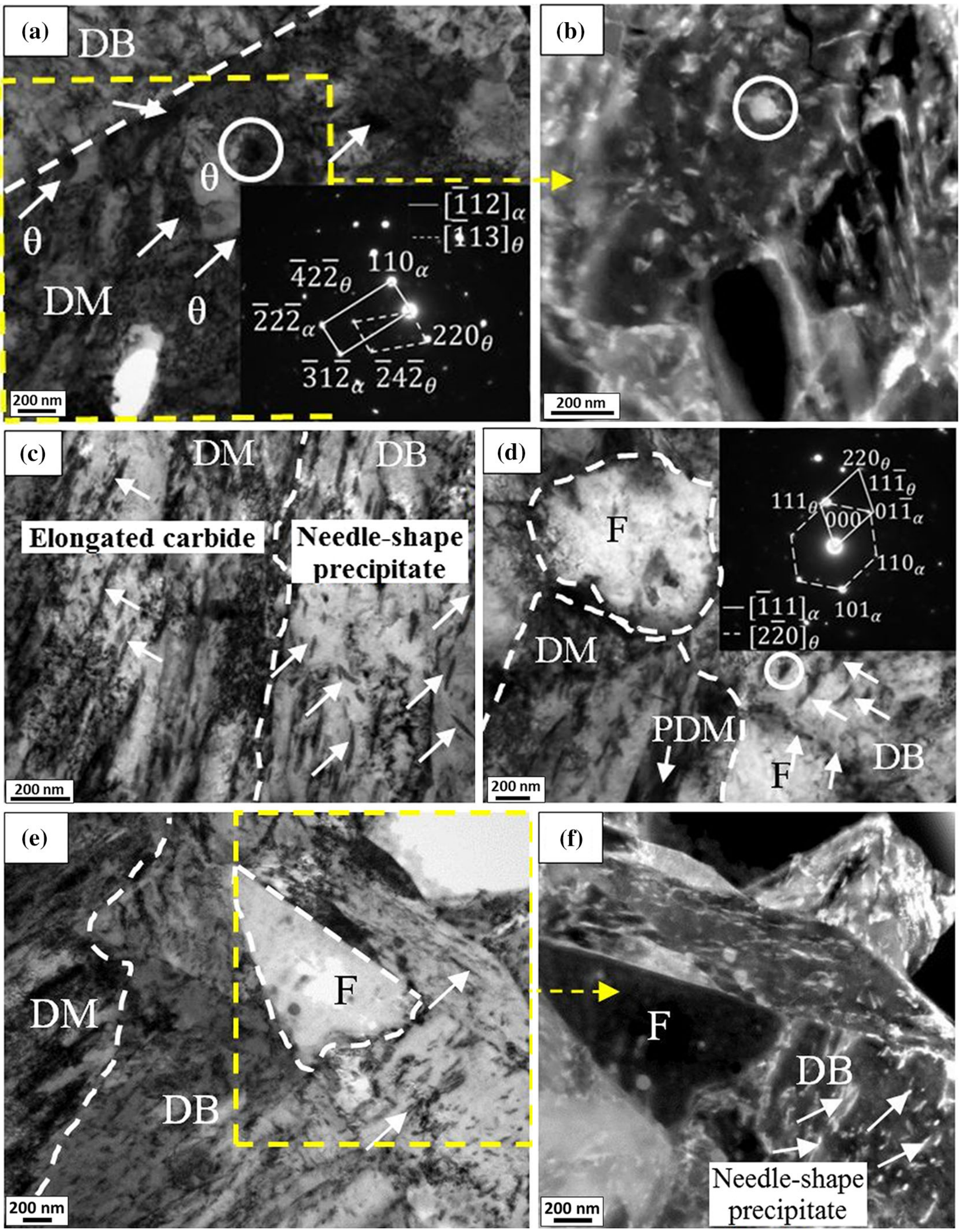

Fig. 8—DP780 steel isothermally tempered at 773 K (500 °C) for 0.5-s duration showing (*a*) spheroidized precipitates in the DM, (*b*) STEM images of selected rectangle in (a), (*c*), and (*d*) interlath elongated cementite in the DM, and needle-shaped precipitates in the DB, (*e*) bright-field micrographs of DM, DB, and F structures, and (*f*) HAADF-STEM image of the DB structure showing needle-shaped carbides (bright contrast, higher atomic level).

austenite films originally found in the interlath boundaries of martensite laths. This observation agrees with those by Baltazar Hernandez *et al.*[4] Partial decomposed martensite (PDM) was also observed. The presence of PDM indicates that there was insufficient time to complete the tempering reaction. Unlike the spherical carbides seen in the DM, the carbides formed in the decomposed α_b were predominantly needle-shaped and uniformly distributed throughout the DB structure (Figures 8(d), (e), and (f)). In addition to needle-shaped carbides, irregular θ-carbides (marked with the circle in Figure 8(d)). The irregular θ-carbides had $[\bar{1}11]_\alpha \| [2\bar{2}0]_\theta$ orientation relationship with the α-matrix. The α-phase observed in the DB structure (Figures 8(d), (e) and (f)) was free from carbides as in the as-received α phase (Figure 5(a)). When the DB was imaged using HAADF (Figure 8(f)), the needle-shaped carbides showing brighter contrast, indicating that they were composed of higher atomic weight elements. This was confirmed by EDX analysis, which indicated that these were M_2C type carbides, where M corresponds to Fe, Mn, and/or Mo. The M_2C carbides (Figure 10) in the DM precipitated at the expense of the orthorhombic θ-carbide particles presents in the as-received steel (Figure 6(c)). During tempering, the Fe atoms within the cementite (Fe_3C) were substituted by strong carbide-forming elements (Cr and Mo in the examined steel), eventually forming M_2C carbides.[16,36,37] The formation of M_2C carbides within the material structure leads to an increase in the

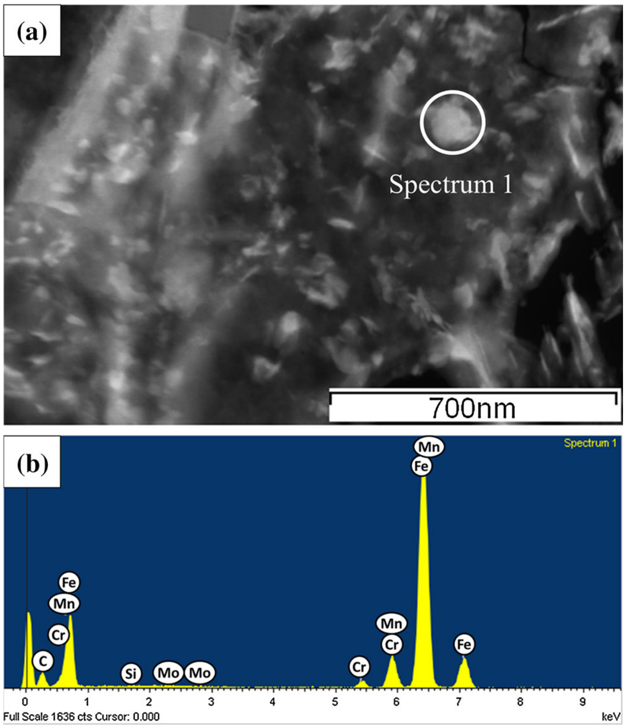

Fig. 9—(*a*) HAADF image illustrating a spheroidized cementite precipitate in the DM and (*b*) the corresponding EDX spectrum of the cementite confirming its Fe, Mn, and Cr contents. The EDX analysis indicated that cementite has a stoichiometric of $(Fe0.87Mn0.11Cr0.02)_3C$.

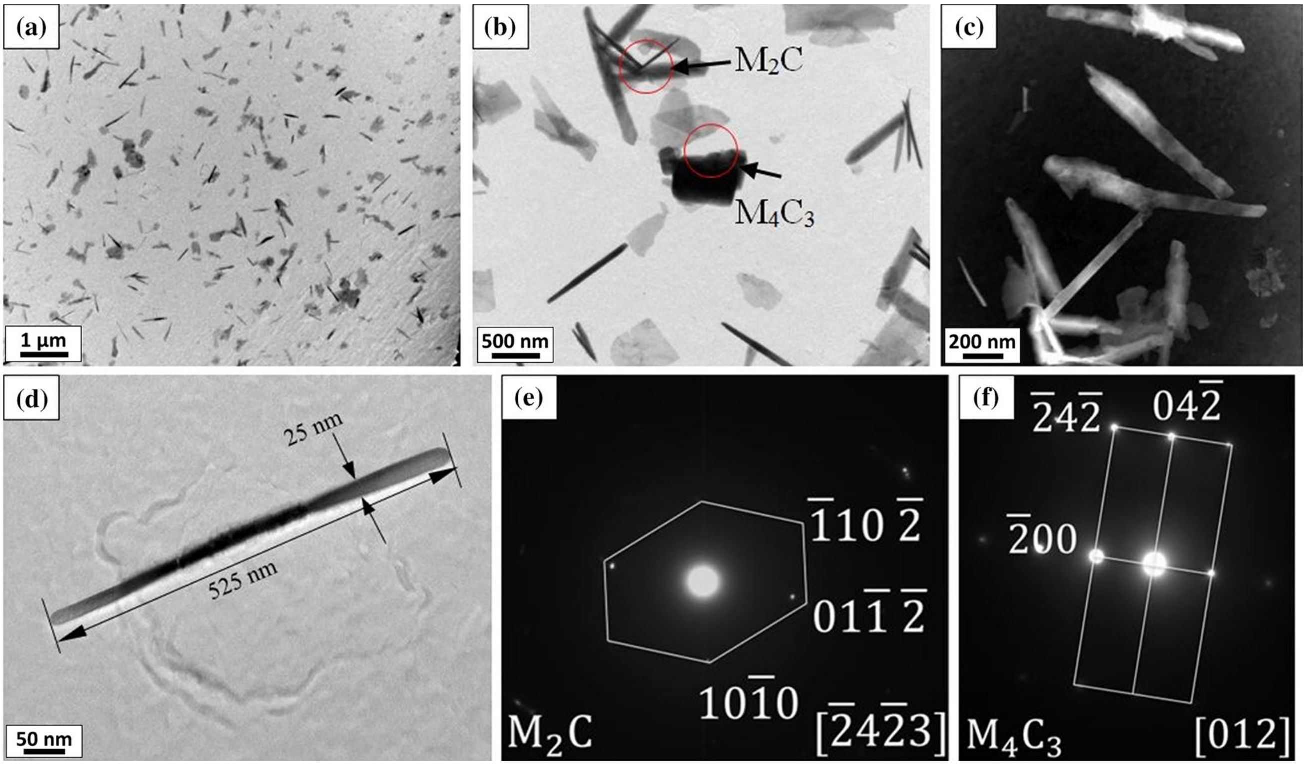

Fig. 10—TEM images (carbon replica) of the alloy carbide particles found in the isothermally tempered DP780 steel samples at 773 K (500 °C) for 0.5-s duration: (*a*) and (*b*) bright-field images with dispersedly distributed alloy carbides M_2C and M_4C_3; (*c*) HAADF-STEM images of the alloy carbides showing higher atomic resolution (bright contrast); (*d*) a single needle-shape M_2C carbide; and (*e*) and (*f*) corresponding indexed SAD for M_2C and M_4C_3 marked on (b).

hardness, *i.e.*, secondary hardening peak (Figures 3 and 4). Fine M_2C-type carbides are precipitated by the dissolution of M_3C-type cementite when the material is aged at 773 K (500 °C). M_2C-type carbides have needle-shaped morphology with a HCP crystal structure,[36,38] which is consistent with Figure 10.

Once identified, the distribution, size, and structure of the needle-shaped precipitates were measured by analyzing images from carbon replicas. The volume fractions of needle-shaped precipitates were measured (using ImageJ software) and found to be ranging from 25 to 30 pct (Figures 10(a) and (b)). HAADF was used to image individual precipitates as shown in Figure 10(c), which were measured. Figure 10(d) shows a single elongated needle-shaped precipitates having a length and a width of 525 and 25 nm, respectively. The aspect ratio of the observed needles was estimated to be ranging from 10 to 25. The SAD pattern taken from one of the needles (Figure 10(e)) indicates that it has an HCP crystal structure with the lattice parameters of a = 2.88 Å and c = 4.76 Å. The measured lattice parameter values were in good agreement with the lattice parameters of Mo_2C (a = 3.0 Å and c = 4.72 Å) as reported by Yamasaki and Bhadeshia[36] It should be noted that the lattice parameters measured by electron diffraction is only accurate to 0.1 pct (as calibrated with standard Au sample). This analysis definitively indicates that Mo_2C is distributed throughout the DB structure. It is well known that the precipitation of the Mo_2C provides secondary hardening peak-tempered high-speed steels.[39] The secondary hardening is due to the coherent precipitation of these carbides,[40] which increases the initial flow stress, resulting in the observed increase in hardness.[41]

In the high-magnification images of the replicas seen in Figures 10(a) and (b), additional plate-shaped precipitates are observed, which could not be resolved in the bulk specimens (Figure 8(d)). A SAD pattern taken from these precipitates (Figure 10(f)) was indexed as the [012] zone axis of a FCC structure having a lattice parameter of 4.30 Å. The plate-shaped precipitates exhibited a lattice parameter close to that of M_4C_3 (for V_4C_3, a = 4.20 Å)-type carbides, where M implies the alloying elements such as V, Fe, and Mn. The difference between the measured and standard values for the lattice parameter was again due to the replacement of V by other elements in this particular material. Pearson[42] observed that the lattice parameter decreases as the V:C ratio increased. As with the M_2C, the observed M_4C_3 precipitated at the expense of θ-carbides, and it may, therefore, be predicted that the θ-carbides present in the untempered materials transformed into the plate-shaped M_4C_3 carbide during the tempering. Again, V is a strong carbide-forming element, and so during tempering at 773 K (500 °C), the Fe atoms in the θ-carbide are substituted by the V atoms, to form stable alloy carbides, which were also responsible for the secondary hardening (Figures 3 and 4).

It can be stated that Mo_2C carbides were formed at the expense of θ-carbides present in the bainite structure of the DP780 steel, which resulted in the secondary hardening. The TiC and M_3C present in the as-received DP780 steel, which were enriched with Mo and V, transformed to form M_4C_3 first and then dissolve *in situ* to provide free carbon to form molybdenum-rich M_2C precipitates.[16] Bhadeshia[16] reported that M_2C-type carbides are formed within the bainite plates in contrast to the formation of a mixture of carbides at the bainite plate boundaries. Since high-angle boundaries are strong heterogeneous nucleation sites, these locations are preferred for nucleation of the alloy carbides. In the present study, the location of the needle-shaped M_2C precipitates were also identified within the bainitic ferrite plates as shown in Figures 8(d) and (f).

During tempering, the Fe atoms in the metastable cementite were replaced by the substitutional solute atoms to form the alloy carbides. Once the alloy carbide precipitated, the secondary hardening peak was observed. It is reported that softening in steels can be reduced by precipitation of ε-copper and other carbides, nitrides, and/or carbonitrides of V, Nb, and Mo.[43] However, further tempering of the steels coarsened the carbides, and they lost coherency with the matrix, decreasing the hardness.[16,44,45] This trend in hardness is seen as shown in Figures 3 and 4, where a hardness peak was seen at moderate levels of tempering; then as tempering progressed (either by tempering at higher peak temperatures or longer durations), the hardness decreased as the carbides continued to coarsen. It must be noted that secondary hardening was observed only in bainite-containing steel because the time necessary for hardening was too short for M_2C and M_4C_3 to form in the tempered martensite. The orthorhombic θ-carbides present in the bainite structure meant that fewer transformations needed to occur to precipitate coherent M_2C carbides, effectively accelerating the onset of secondary hardening. Without pre-existing θ-carbides in the structure, longer tempering times are needed before secondary hardening can be observed.[36]

IV. CONCLUSIONS

In this study, the secondary hardening identified in rapid tempering, *i.e.*, Gleeble tempering and laser welding of microalloyed DP780 steel with ferrite, martensite, and bainite microstructures were investigated. The hardness profile in the laser welds agreed well with those of calculated plots of hardness *vs* HJ tempering parameter, suggesting that secondary hardening occurred in the steel when tempered at 773 K (500 °C). Secondary hardening was due to transformations of the pre-existing carbides found within the bainite structure. Within the bainite, the pre-existing cementite Fe_3C, and TiC were dissolved at high temperature to act as a carbon source to form plate-shaped M_4C_3 and needled-shape M_2C carbides, which led to secondary hardening in the Gleeble specimen tempered at 773 K (500 °C) for 0.5 second. The isothermal tempering products strongly correlate with the hardening peak observed in the HAZ of the DP780 steel laser welds. However, this phenomenon is not likely to occur in bainite-free DP780 steels where no such θ-carbides are available to transform into secondary hardening carbides during rapid tempering and welding.

REFERENCES

1. R. Nadlene, H. Esah, S. Norliana, and M.A. Mohd Irwan: *World Acad. Sci. Eng. Technol.*, 2011, vol. 50, pp. 564–67.
2. C. Yao, B. Xu, J. Huang, P. Zhang, and Y. Wu: *Opt. Laser Eng.*, 2010, vol. 48, pp. 20–26.
3. S.S. Nayak, V.H. Baltazar Hernandez, and Y. Zhou: *Metall. Mater. Trans. A*, 2011, vol. 42A, pp. 3242–48.
4. V.H. Baltazar Hernandez, S.S. Nayak, and Y. Zhou: *Metall. Mater. Trans. A*, 2011, vol. 42A, pp. 3115–29.
5. E. Biro and A. Lee: *Sheet Metal Welding Conference XI*, Sterling Heights, MI, 2004.
6. T. Burns: Master Thesis, University of Waterloo, 2009.
7. M. Xia, E. Biro, Z. Tian, and Y. Zhou: *ISIJ Int.*, 2008, vol. 48, pp. 809–14.
8. P. Ghosh: *ISIJ Int.*, 1990, vol. 30, pp. 317–24.
9. V.H. Baltazar Hernandez, S.K. Panda, Y. Okita, and Y. Zhou: *J. Mater. Sci.*, 2010, vol. 45, pp. 1638–47.
10. H. Tanabe, A. Miyasaka, I. Anai, and S. Tanioka: *Nippon Steel Tech. Rep.,* 1995, pp. 62–68.
11. M. Jung, S.-J. Lee, and Y.-K. Lee: *Metall. Mater. Trans. A*, 2009, vol. 40A, pp. 551–59.
12. G.B. Olson and W.S. Owen: *Martensite*, Metals Park, OH, ASM International, 1992, p. 261.
13. R.C. Thomson and M.K. Miller: *Acta Mater.*, 1998, vol. 46, pp. 2203–13.
14. D. Huang, S.S. Nayak, M.A. Wells, Y. Zhou, and E. Biro: *Sheet Metal Welding Conference XV Proceedings*, MI, Livonia, 2012, pp. 1–11.
15. A.D.B. Gingell, H.K.D.H. Bhadeshia, D.G. Jones, and K.J.A. Mawella: *J. Mater. Sci.*, 1997, vol. 32, pp. 4815–20.
16. H.K.D.H. Bhadeshia: *Bainite in Steels: Transformations Microstructure and Properties*, IOM Communications Ltd., London, 2001.
17. D. Delagnes, P. Lamesle, M.H. Mathon, N. Mebarki, and C. Levaillant: *Mater. Sci. Eng. A*, 2005, vol. 394, pp. 435–44.
18. C.H. Yoo, H.M. Lee, J.W. Chan, and J.W. Morris, Jr: *Metall. Mater. Trans. A*, 1996, vol. 27A, pp. 3466–72.
19. D. Rosenthal: *Weld. J.*, 1941, vol. 20, p. 220s.
20. A.K. Jena and M.C. Chaturvedi: *Mater. Sci. Eng.*, 1988, vol. 100, pp. 1–6.
21. N. Saeidi and A. Ekrami: *Mater. Sci. Eng. A*, 2009, vol. 523, pp. 125–139.
22. F. Danoix, R. Danoix, J. Akre, A. Grellier, and D. Delagnes: *J. Microscopy*, 2011, vol. 244, pp. 305–10.
23. J.H. Hollomon and L.D. Jaffe: *Trans. TMS-AIME*, 1945, vol. 162, pp. 223–49.
24. D. Kuhlmann-Wilsdorf: *Metall. Trans. A*, 1985, vol. 16A, pp. 2091–108.
25. W. Saikaly, X. Bano, C. Issartel, G. Rigaut, L. Charrin, and A. Charai: *Metall. Mater. Trans. A*, 2001, vol. 32A, pp. 1939–47.
26. J.H. Jang, C.-H. Lee, H.N. Han, H.K.D.H. Bhadeshia, and D.-W. Suh: *Mater. Sci. Technol.*, 2013, pp. 1–6.
27. K. Nishioka and K. Ichikawa: *Sci. Technol. Adv. Mater.*, 2012, vol. 13, pp. 1–20.
28. G.K. Tirumalasetty, C.M. Fang, Q. Xu, J. Jansen, J. Sietsma, M.A. Huis, and H.W. Zandbergen: *Acta Mater.*, 2012, vol. 60, pp. 7160–68.
29. K. Aigner, W. Lengauer, D. Rafaja, and P. Ettmayer: *J. Alloy. Compd.*, 1994, vol. 215, pp. 121–26.
30. W. Kim, J. Park, C. Suh, S. Cho, S. Lee, and I.-J. Shon: *Mater. Trans.*, 2009, vol. 50, pp. 2897–99.
31. H.A. Wriedt and J.L. Murray: *Bull. Alloy Phase Diagr.*, 1987, vol. 8, pp. 378–88.
32. Y. Kang, Q. Han, X. Zhao, and M. Cai: *Mater. Des.*, 2013, vol. 44, pp. 331–39.
33. J.M. Schissler, J. Arnould, and G. Metauer: *Mem. Sci. Rev. Metall.*, 1975, vol. 6, pp. 779–93.
34. J.H. Jang, I.G. Kim, and H.K.D.H. Bhadeshia: *Comput. Mater. Sci.*, 2009, vol. 44, pp. 1319–26.
35. T. Furuhara, K. Kobayashi, and T. Maki: *ISIJ Int.*, 2004, vol. 44, pp. 1937–44.
36. S. Yamasaki and H.K.D.H. Bhadeshia: *Mater. Sci. Technol.*, 2003, vol. 19, pp. 723–31.
37. D. Delagnes, F. Pettinari-Sturmel, M.H. Mathon, R. Danoix, F. Danoix, C. Bellot, P. Lamesle, and A. Grellier: *Acta Mater.*, 2012, vol. 60, pp. 5877–88.
38. T.P. Hou, Y. Li, Y.D. Zhang, and K.M. Zu: *Metall. Trans. A*, 2014, vol. 45A, pp. 2553–61.
39. A.-M.E. Rakayby and B. Mills: *Mater. Sci. Technol.*, 1986, vol. 2, pp. 175–80.
40. Z. Hu, X. Wu, and C. Wang: *Mater. Sci. Technol.*, 2004, vol. 20, pp. 425–28.
41. M.S. Bhat, W.M. Garrison, Jr., and V.F. Zackay: *Mater. Sci. Eng.*, 1979, vol. 41, pp. 1–15.
42. W.B. Pearson: *A Handbook of Lattice Spacings and Structures of Metals and Alloys*, Pergamon Press, Oxford, 1958, pp. 895–1037.
43. J. Koo and M. J. Luton: United Nations Patent, 5545269, 1996.
44. C.H. Yoo, H.M. Lee, J.W. Chan, J. Morris, and W. John: *Metall. Mater. Trans. A*, 1996, vol. 27A, pp. 3466–72.
45. K. Cho, J. Choi, H. Kang, S. Kim, K. Lee, H. Yang, and H. Kwon: *Mater. Sci. Eng. A*, 2010, vol. 527, pp. 7286–93.